Steady-state, simultaneous two-phase flow in porous media: experiment and simulation

Ken Tore Tallakstad,[1,*] Grunde Løvoll,[1,†] Thomas Ramstad,[2,‡]
Henning Arendt Knudsen,[1] Knut Jørgen Måløy,[1] and Alex Hansen[2]

[1] *Department of Physics, University of Oslo, PB 1048 Blindern, NO-0316 Oslo, Norway*
[2] *Department of Physics, Norwegian University of Science and Technology, NO-7491 Trondheim, Norway*

(ΩDated: December 18, 2007)

We report on experimental and numerical studies of steady-state two-phase flow in a quasi two-dimensional porous medium. Experimentally, the wetting and the non-wetting phase are injected simultaneously from alternating inlet points into a Hele-Shaw cell containing one layer of randomly distributed glass beads, initially saturated with wetting fluid. Transient behavior is observed in time and space, such that at a certain distance behind the front, fully developed fragmented steady-state flow develops. Numerical studies confirm this transition and support the conclusion that the steady-state phase is fragmented and dominated by bubble dynamics, allowing for a statistical description on the meso-scopic scale in terms of effective behavior and on the micro-scale in terms of cluster-size distributions. The latter is shown to obey a scaling-law with the Darcy velocity.

I. INTRODUCTION

Payatakes et al. should be mentioned!?

II. EXPERIMENTAL SETUP

The experimental setup is shown in Figs. 1 and 2. The porous model consists of a mono-layer of glass beads of diameter $a = 1$ mm which is randomly spread between two contact papers [1, 2]. The model is a transparent rectangular box of dimensions $L \cdot W = 850 \cdot 420$ mm^2 and thickness a.

A 2 cm thick Plexiglas plate is placed on top of the model. To squeeze the beads and the contact paper together with the upper plate, a mylar membrane mounted on a 2.5 cm thick Plexiglas plate, below the model, is kept under a 3.5 m water pressure as a "pressure cushion". The upper and the lower plate are kept together by clamps, and the side boundaries are sealed by a rectangular silicon rubber packing. The upper plate have 15 drilled independent inlets for fluid injection and a milled outlet channel (Fig. 2). The distance between the inlets and the outlet channel define the length of the model $L = 850$ mm. The porosity of the model is measured to be $\phi = 0.63$ and the permeability is $\kappa = (0.0195 \pm 0.001) \cdot 10^{-3}$ cm^2 $= (1980 \pm 100)$ Darcy.

The wetting fluid used in all our experiments is a 85%−15% by weight *glycerol-water* solution dyed with 0.1% Negrosine to increase the contrast between the colored fluid and the invader. *Air* is used as the non-wetting fluid. The *wetting* glycerol-water solution has a viscosity of $\mu_w \approx 0.11$ Pa.s and a density of $\rho_w = 1217$ kg.m^{-3} at room temperature. The corresponding parameters for the *non-wetting* air are $\mu_{nw} = 1.9 \cdot 10^{-5}$ Pa.s and $\rho_{nw} = 1.168$ kg.m^{-3}. The viscous ratio is thus $M = \mu_{nw}/\mu_w \sim 10^{-4}$. The surface tension between these two liquids is $\gamma = 6.4 \cdot 10^{-2}$ N.m^{-1}. The temperature in the defending fluid is controlled and measured at the outlet of the model during each experiment, so as to accurately estimate the viscosity of the wetting fluid.

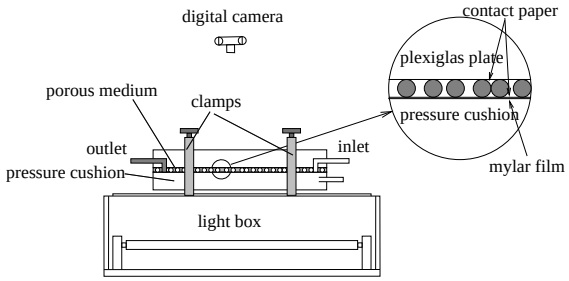

FIG. 1: *Sketch of the experimental setup with the light box for illumination, the porous model and the digital camera. The porous medium is sandwiched between two contact papers and kept together and temperature controlled with a water filled "pressure cushion".*

During experiments the absolute pressure is recorded at four different positions. In one of the air inlet tubes and in the wetting fluid at the edge of the model: close to the inlet, at a distance $L/2$ in the flow direction and in the outlet channel (Fig. 2) using *SensorTechnics 26PC0100G6G Flow-Through* pressure sensors.

The flow structure is visualized by illuminating the model from below with a light box and pictures are taken at regular intervals with a *Pixelink Industrial Vision PL-A781* digital camera, which is controlled by a computer over a FireWire connection. This computer records both the pictures and the pressure measurements. Each image contain 3000×2208 pixels, which corresponds to a spatial resolution of ~ 0.19 mm per pixel (27 pixels in a pore of size 1 mm^2). The color scale contains 256 Gray levels.

*k.t.tallakstad@fys.uio.no
†grunde.lovoll@fys.uio.no
‡Thomas.Ramstad@phys.ntnu.no

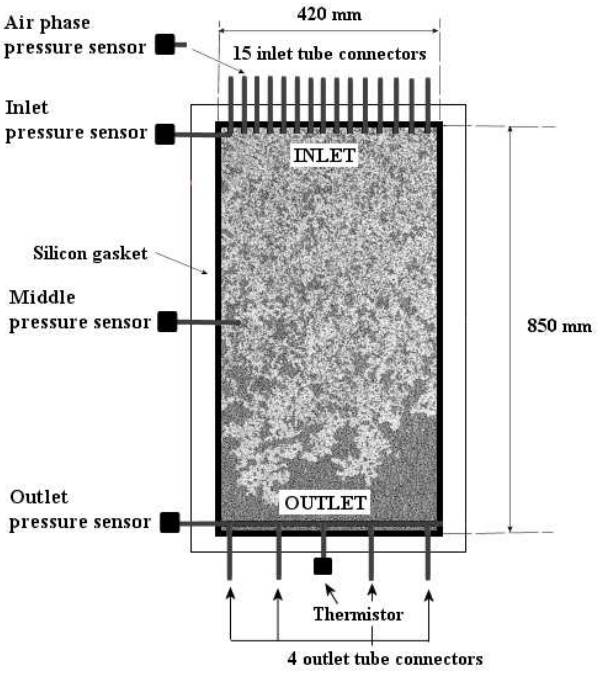

FIG. 2: *Sketch of the experimental model. With the* 15 *independent inlet holes with attached tubes where we inject (alternating) wetting and non-wetting phase with syringe pumps. This leads to mixing of the two phases inside the model two dimensional porous media (random mono layer of glass beads) and a mix of the two phases flows out of the outlet channel in the opposite end of the system. In one of the inlet tubes (non-wetting phase) and in the porous model (wetting phase) pressure sensors are mounted for pressure measurements.*

The Gray level distribution of the image presents two peaks corresponding respectively to the white air-filled and dark gray glycerol-filled parts of the image. The image is thresholded at a constant offset from the white-peak so as to obtain a representative boundary between the two phases [3]. All further image treatments are performed on the resulting black and white image. Analysis has shown that the extracted results display only small deviations to perturbations of the chosen threshold value.

In all experiments the porous model is initially filled with the wetting glycerol-water solution. An experiment is then started by injecting non-wetting and wetting fluid from every other inlet hole (Fig. 2). The wetting (glycerol-water) and non-wetting (air) fluid is thus injected using individual syringe pumps, all set at equal displacement rate, from 8 and 7 of the 15 inlet holes respectively.

III. SIMULATION MODEL

This section will contain a brief résumé of the network model used in the simulations. Detailed descriptions are found in the work by Aker *et al.* and Knudsen *et al.*[4, 5]. More compact descriptions are found in later work by Knudsen and Hansen[6] and Ramstad and Hansen[7].

A. Boundary conditions

In simulations the boundary conditions may be chosen more freely than what is the case in the experiments. Let the porous medium itself be a two-dimensional network of tubes. Allowing one side to serve as inlet row and the opposite side to serve as outlet row, an invasion process may be simulated. On the sides, parallel to the direction of flow, the boundaries are periodically connected. This reduces boundary effects, thus making the system more alike a system larger than its actual size.

In this particular study wetting and nonwetting fluid have been injected alternately through points in the inlet row. This is so in order to allow for a direct comparison with experiment. Of particular interest is to study the transient to steady-state and the steady-state itself. Bi-periodic boundary conditions, connecting outlet with inlet, close the system and create a flow state that evolves into steady-state by construction. Eventually, the story will be completed with some considerations about the nature of steady-state in the two cases.

IV. RESULTS

As the non-wetting liquid enters the model it first forms elongated clusters which are connected to the respective inlets. As these clusters grow they are snapped off by the wetting fluid and transported as bubbles along the flow towards the outlet of the model. Over time the non-wetting air clusters propagate all the way to the outlet of the model, thus filling the whole porous matrix with a mixture of air and glycerol-water solution. The air only exists in the form of fragmented clusters while the glycerol-water solution percolates the model at all times. It is observed both in experiments and simulations that the smallest air clusters usually are immobile and trapped, whereas larger clusters are mobile and propagate in the porous medium. However, trapped clusters can be mobilized when they coalease with larger migrating clusters. On the other hand, migrating clusters can be fragmented and thereby trapped. The fate of an air cluster is thus highly undecided.

We run the experiment for a significant time after air break through. Shortly after breakthrough the transport process is in steady-state, meaning that both phases are transported trough the model without “long time” flow parameter changes; implying that the pressure difference, relative permeabilities, saturations and cluster distributions are on average constant. Images of the evolution of the transient part of a typical experiment is shown in the right column of Fig. 13.

In Fig. 3 the absolute pressure is plotted as function of time for three positions. We can see the “break through”

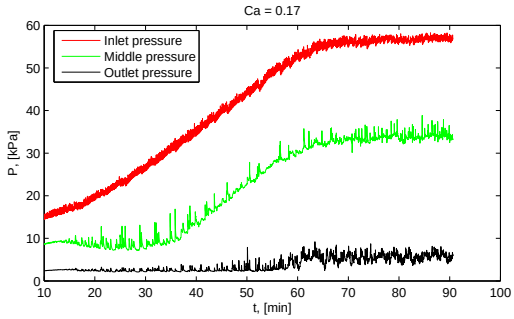

FIG. 3: *Example of pressure evolution at different positions in the model as function of time.*

at $t \simeq 60$ min in the pressure signal from the outlet channel. Shortly after this the signal from the other two sensors approach a constant level as we reach steady-state. In the transient regime the overall pressure behavior at the three sensors appears different. As air enters the model the pressure near the inlet start to increase and it increases linearly until breakthrough, while the pressure in the middle sensor is constant until the air bubbles reach the sensor ($\sim$ 30 min). At this point the middle sensor pressure also start to increase linearly. This is because the average pressure at a point inside the porous medium is controlled by the viscous pressure drop between that point and the outlet channel. And as air bubbles passes the sensor the effective permeability of the media in front of the sensor is lowered, and to maintain constant flow rate the pressure have to increase. The pressure in the outlet channel fluctuates around zero until t_{ss} is reached, after which a jump to the constant steady-state level is seen.

To learn more about the transient and the transition to steady-state, we here present the results of six experiments, performed at different injection rate. The injection rate is controlled by the speed of the step motor used to control the syringe pumps. The rates and the corresponding capillary number are given in table I. We define the capillary number as

$$\mathrm{Ca} = \frac{\mu_w Q_w a^2}{\gamma \kappa A} \ , \qquad (1)$$

where $A = W \cdot a$ is the cross-sectional area and Q_w=8Q_0 is total flow rate of the wetting fluid.

A. Transient behavior

A first characteristic time in the transient regime is the elapsed time from onset of invasion until the first breakthrough of nonwetting fluid (air). Recall that the model initially is filled with wetting fluid. We determine this breakthrough time t_b by visual inspection in each experiment. A second characteristic time is when all signs of transient behavior vanish; the steady-state time t_{ss}. To some degree it is possible to see the transition to steady-state also by visual inspection. However, as opposed to the breakthrough time, which is sharply defined visually, the steady-state time is not so sharply defined in this way.

Ca	Q_0(ml/min)	$15Q_0$(ml/min)	Q_{tot}^{inv}(ml/min)
0.17	0.553	8.29	5.73
0.090	0.279	4.18	2.90
0.032	0.114	1.71	1.29
0.015	0.055	0.83	0.67
0.0079	0.023	0.41	0.35
0.0027	0.011	0.16	0.15

TABLE I: For each of six experiments are given: the capillary number, the corresponding flow rate out of a single syringe pump Q_0, the total flow rate $15Q_0$, and the total invasion flow rate Q_{tot}^{inv}. The difference between $15Q_0$ and Q_{tot}^{inv} is due to compressibility effects as discussed in Sec. IV D. The capillary number is calculated from Eq. (1).

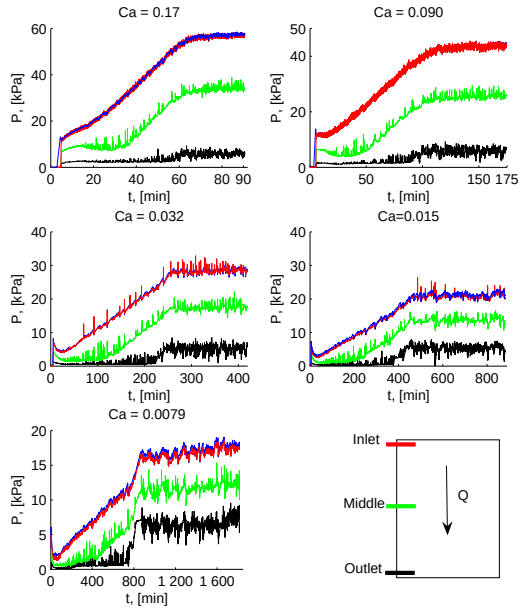

FIG. 4: *Time evolution of the pressure in each of five different experiments, performed at different injection rate, which is denoted in terms of the capillary number. The pressure is measured at the inlet, in the middle, and near the outlet, as depicted in the lower right panel.*

In order to quantize the steady-state time, we make use of the measured pressure curves. Fig. 4 shows the pressure evolution at three different points: inlet, middle, and outlet for each experiment. The pressure saturates and fluctuates around some value for long times in all cases. Prior to saturation there is a period of close to linear increase in the pressure. By making a straight line fit to this slope and flat line fit to the saturated value, we

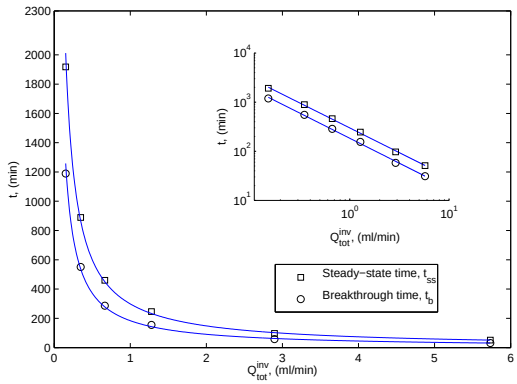

FIG. 5: *Measured breakthrough time t_b and steady-state time t_{ss} as a function of the total invasion flow rate Q_{tot}^{inv}.*

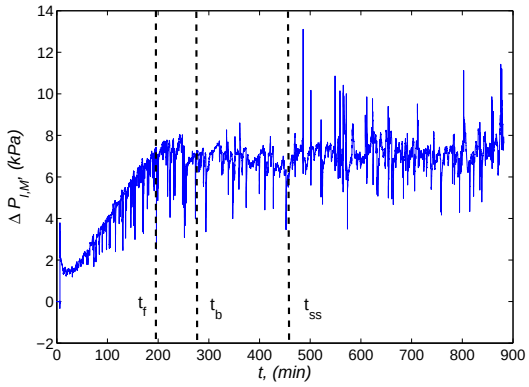

FIG. 6: *Pressure difference between inlet and middle-sensor $\Delta P_{I,M}$ as a function of time t for $Ca = 0.015$. Three characteristic times are indicated by dashed lines; the time at which the front passes the middle sensor t_f, the breakthrough time t_b and steady-state time t_{ss}.*

define their crossing point to be the steady-state time t_{ss}. This definition is sharp and consistent in the sense that this time is the same no matter which of the pressure measurement points(inlet or middle) is used. The outlet measurement is less good for this purpose due to the very short period of pressure rise before saturation.

The resulting characteristic times are plotted in Fig. 5. Power law fits are shown in the inset. By assuming that the times obey the form

$$t_b = V_b \left(Q_{tot}^{inv}\right)^{-\alpha_b} \tag{2}$$

$$t_{ss} = V_{ss} \left(Q_{tot}^{inv}\right)^{-\alpha_{ss}} \tag{3}$$

as a function of the flow rate, one gets

$$\alpha_b = \alpha_{ss} = 1.01 \pm 0.05 \ . \tag{4}$$

This result is consistent with an exponent 1. The two pre-factors V_b and V_{ss} have units of volume, and may be directly interpreted as displaced volumes at the respective times.

From the above data we calculate the relative time difference between t_b and t_{ss}. This gives

$$\frac{t_{ss} - t_b}{t_b} = \frac{V_{ss} - V_b}{V_b} = 0.62 \ . \tag{5}$$

Here we used the fact that $t_b \times Q_{tot}^{inv} = V_b$ and $t_{ss} \times Q_{tot}^{inv} = V_{ss}$. Eq. (5) states that the time difference between breakthrough and steady-state, for all experiments, is 38% of the breakthrough time.

B. Steady-state

In Sec.IV A we learned that there exists a well defined transition to steady-state based upon analysis of the pressure signal. This is a global criterion, meaning that the system as a whole has reached a steady-state. We wish to look at this also on a local scale.

From the onset of invasion a frontal region establishes where nonwetting fluid clearly is moving forward in a band, see Fig. 13. This band contains quite large nonwetting clusters and the nonwetting saturation is somewhat larger than compared to the region behind the frontal region. In addition the region behind the front is more fragmented and homogeneous. We claim that locally, the region behind the front has already entered into steady-state. This is interesting because this happens very early in the process. Gradually more and more of the model enters into this state as the frontal region with more nonwetting fluid sweeps through the model towards the outlet. Two arguments support this observation.

Firstly, there is the fact that the middle sensor pressure increases linearly from the time t_f right after the front has reached the sensor. The linear increase is at the same slope as the inlet sensor pressure; a behaviour which sustains until steady-state is reached globally. For all experiments we find that the pressure difference between the inlet- and middle-sensor, $\Delta P_{I,M}(t_f < t < t_{ss})$ during this linear increase is hardly distinguishable from $\Delta P_{I,M}(t > t_{ss})$, as shown in Fig. 6. Since the displacement rate is constant and close to equal both in the transient- and steady-state, it follows from Fig. 6 that the relative permeability of the region behind the front must equal that of later global steady-state.

Secondly, we have performed image analysis of parts of the model behind the front in the transient regime as well as in global steady-state. It turned out that both saturation measurements and cluster size distributions were in agreement in the two cases. This statistical equality and the above results can hardly be achieved unless the region behind the front is in local steady-state.

The global steady-state can be quantized by: the averaged global pressure drop between the inlet and outlet ΔP_{ss} and the non-wetting fluid saturation S_{nw}, see Fig. 7a and b.

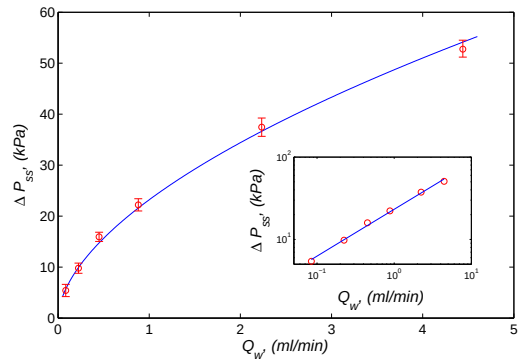

(a)

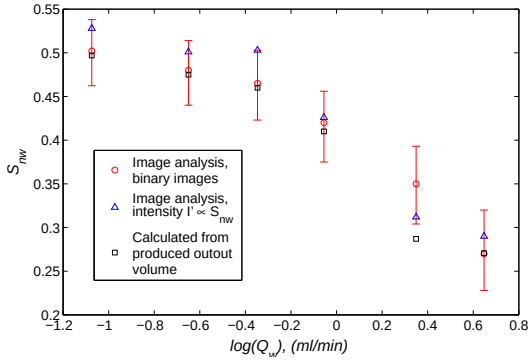

(b)

FIG. 7: ***(a)*** *Plot of the pressure difference.* ***(b)*** *saturation as function of the tuning parameter* Q_w.

One observes that the nonwetting saturation decreases with increasing total injected flow rate. Since the nonwetting fluid is air and hence much less viscous than the wetting fluid, it is intuitively correct that it needs to occupy a smaller part of the pore space to obtain a certain flow rate when the speed is increased. The reason is its much higher ability to move, combined with the lesser importance of capillary barriers, briefly speaking. (Authors' NOTE: it is appropriate to elaborate more on this point, possibly include some words about simulations in this context.)

The pressure scales with a power law in the flow rate, as shown in the inset of Fig. 7. In numbers we get

$$\Delta P_{ss} \propto Q_w^{\beta} \ , \tag{6}$$

with the exponent

$$\beta = 0.57 \pm 0.08 \ . \tag{7}$$

This behavior is by no means obvious, in particular the fact that the exponent appears to be nontrivial is intriguing. We will return to a physical interpretation of this result in Sec.IV C.

C. Cluster size distributions

After the systems have entered into steady-state, we have analyzed images of the structure in order to determine the size distribution of non-wetting clusters or bubbles. The normalized distributions $P(s)$ as a function of cluster size s for all Ca-numbers investigated are shown in Fig.8a. A trivial observation is the decrease in probability with increasing cluster size. Less obvious is the fact that the curves show an exponential-like cut-off depending on the capillary number. Additionally there is a cut-off region for smaller clusters, as the cluster size approaches the bead size. Since the beads are counted as part of the clusters during image analysis, we have no information at this size scale. For the highest Ca-numbers, the whole distribution is dominated by the exponential cut-off. However, as the Ca-number is decreased, a small region of powerlaw-like behaviour is observed in between the two cut-offs.

Analog to what is done in percolation theory [8], we assume that the distribution of the largest clusters follows the function

$$P(s) \propto s^{-\tau} \exp(-s/s^*), \tag{8}$$

where s^* is the cut-off cluster size. The latter function have been fitted, using a proportionality constant, τ and s^* as fit-parameters, to the experimental data for each Ca-number. This is shown by the solid lines in Fig.8a. By averaging the fitted τ exponents it is found that $\tau = 2.07 \pm 0.18$. The uncertainty only reflects the difference in fitted exponents. From the distributions it is seen that no powerlaw-region is well pronounced, and we do not claim that τ is determined with a large degree of certainty in this case. When it comes to the cut-off cluster size the fitted values of s^* are found to scale with Ca (Eq. (1)), hence also with the tuning parameter as

$$s^* \propto Q_w^{-\gamma} \ , \tag{9}$$

where $\gamma = 1.05 \pm 0.07$. This is shown in the inset of Fig. 8b. One should note, even for the lowest Ca-number, that $s^* \sim 10^4$ is considerably smaller than the system size $\sim 10^6$, meaning that large scale finite-size effects should not be of importance. Eq. (8) predicts a re-scaling of the x- and $y-$axis with $1/s^*$ and $s^{*\tau}$ respectively. On this basis the data-collapse in Fig. 8b is obtained.

From the above considerations, the cluster size distribution of non-wetting clusters in steady-state obeys the scaling function

$$P(s) \propto s^{*-\tau} H(s/s^*), \tag{10}$$

where $H(x)$ contains an exponential cut-off (Eq.(8)) so that $P(s) \to 0$ when $x \gg 1$.

Up to now the cluster size measured in area was studied. One step further is to consider the linear extension of the clusters in the two directions l_x - transverse to the overall direction of flow, and l_y - oriented along the

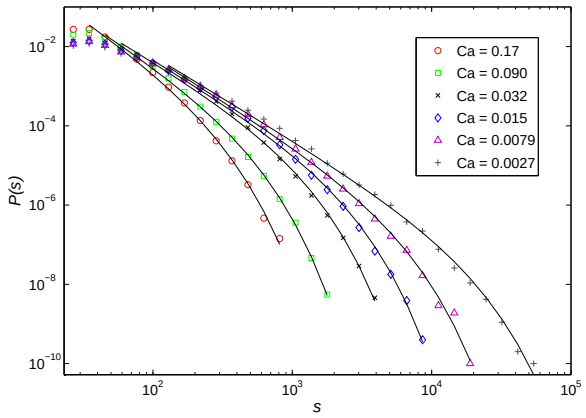

(a)

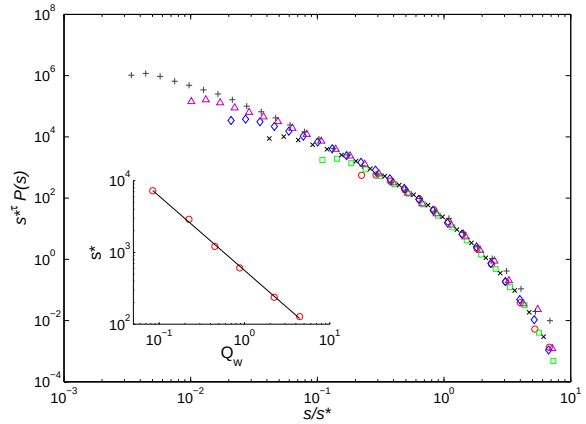

(b)

FIG. 8: *Non-wetting cluster size distribution $P(s)$ in steady-state for all experiments. The cluster size s is measured in pixels; 1 pixel = 0.037 mm^2.* ***(a)*** *Normalized probability distributions. The dominating cut-off behaviour is evident. The solid lines represent fits of Eq.(8).* ***(b)*** *The x- and $y-$axis are re-scaled with $1/s^*$ and $s^{*\tau}$ respectively, to obtain the data collapse. The Q_w dependence of the cut-off cluster size s^* is shown in the inset.*

overall direction of flow. This is achieved by assigning a bounding box of sides l_x and l_y to a cluster of size s, i.e. the smallest rectangle that can contain the cluster. In the following, l_i, where $i \in \{x, y\}$, will denote both the l_x- and l_y-extension. It is found that the distribution of l_i for a given cluster size $s \leq s^*$, $P(l_i|s)$, is a Gaussian. Additionally the corresponding standard deviation σ and mean $\langle l_i \rangle$ scale with the cluster size as

$$\sigma = A_\sigma s^{\beta_\sigma} \tag{11}$$

$$\langle l_i \rangle = A_i s^{\beta_i}, \tag{12}$$

with prefactors $A_\sigma = 0.25$ and $A_i = 1.12$, where $\beta_\sigma = 0.55 \pm 0.06$ and $\beta_i = 0.57 \pm 0.05$. Within the limits of uncertainty, β_σ and β_i can be considered equal. The corresponding prefactors yield that

$$\sigma / \langle l_i \rangle \approx 0.22 \ , \tag{13}$$

meaning that the standard deviation is roughly 22% of the mean extension length.

The collapse of multiple $P(l_i|s)$ distributions of different cluster sizes and Ca-numbers, and the scaling of Eqs. (11,12) are shown in Fig. 9a and b respectively. Fig. 9a reveal a strong correlation between cluster size and linear extension, and we believe that the use of bounding boxes to characterise the clusters are justified. It is evident from Fig. 9b that the scaling of $\langle l_x \rangle$ and

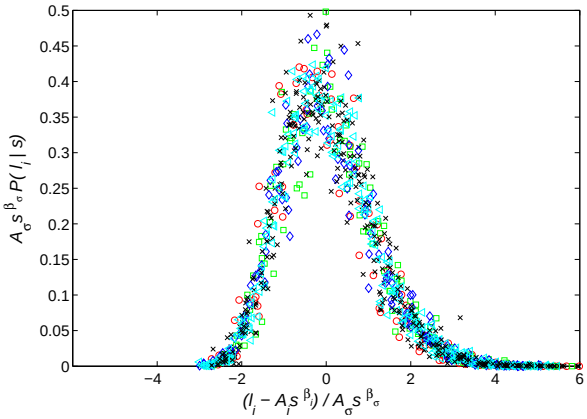

(a)

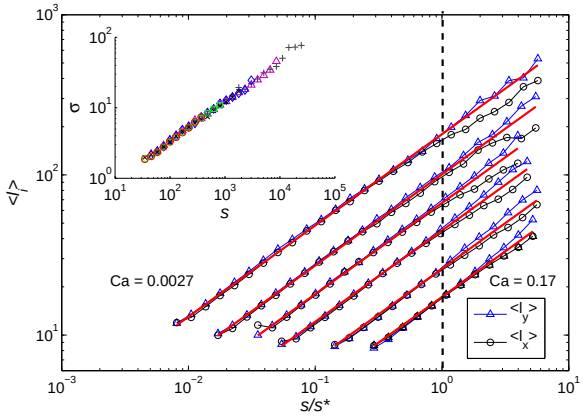

(b)

FIG. 9: *The extension lengths l_i are measured in pixel units; 1 pixel = 0.19 mm.* ***(a)*** *datacollapse of multiple $P(l_i|s)$ distributions. s values are picked from all experiments, and ranges over four decades. The collapse is obtained by a rescaling predicted by the Gaussian distribution function.* ***(b)*** *scaling of $\langle l_y \rangle$ and $\langle l_x \rangle$ with s for all Ca-numbers. The x-axis has been rescaled with $1/s^*$ to emphasise that Eq. (12), represented by the solid lines, does not apply for $s > s^*$. The inset shows the scaling of σ with s, Eq. (11).*

$\langle l_y \rangle$ is equal for $s \leq s^*$, a point to which we will return shortly. However, at this stage we note that the cut-off

cluster size s^* corresponds to a cut-off extension length l^*. From Eqs. (9,12) it follows that

$$l^* = A_i s^{*\beta_i} \propto Q_w^{-\gamma\beta_i} \ . \tag{14}$$

The similar scaling of $\langle l_i \rangle$ for $s \leq s^*$ means that non-wetting clusters fit into quadratic bounding boxes on the average, and can thus be considered isotropic at these sizes. This is seen from Fig. 10 where $\langle l_x \rangle$ is plotted vs. $\langle l_y \rangle$, both rescaled with the cut-off extension length $1/l^*$. It is evident that the average bounding box for $\langle l_i \rangle \leq l^*$ is quadratic, and furthermore this behaviour is independent of Ca. When $\langle l_i \rangle$ reaches l^*, equivalent to the cluster size reaching s^*, there is a crossover and the clusters are seen to be somewhat elongated in the direction of flow on the average. Cluster elongation or an-isotropy is best emphasised by considering the average relative length difference, $\Delta l / \langle l_y \rangle$ where $\Delta l = \langle l_y \rangle - \langle l_x \rangle$. The inset of Fig. 10 shows, for six Ca-numbers, the relative length difference for all cluster sizes. Each curve is characterised by a region where the relative length difference is constant or only slowly increasing, always less than 5%. As the cutoff cluster size s^* is reached $\Delta l / \langle l_y \rangle$ increases significantly. Specifically, the largest sustainable clusters are roughly 30% longer in the direction of flow than transverse to the direction of flow.

To understand elongation one has to consider how the capillary pressure P_{cap} between the two phases in a cluster is affected by a surrounding viscous pressure field. In mechanical equilibrium, the surface pressure equals the capillary pressure

$$P_{nw} - P_w = P_{\text{cap}}. \tag{15}$$

The wetting fluid pressure difference ΔP_w over a cluster of length l_y can be approximated as

$$\Delta P_w \approx \frac{\Delta P_{ss}}{L} l_y, \tag{16}$$

whereas the non-wetting fluid pressure P_{nw} essentially is constant inside the cluster. The capillary pressure over the interface of the cluster will thus decrease in a direction opposite to that of the overall flow; highest at the tip and lowest at the tail of the cluster. As we shall see, this introduces an-isotropy which will depend on the extension length l_y.

In the case of steady-state simultaneous flow, the dynamics of non-wetting clusters are influenced by a competition of *both* drainage and imbibition processes. A pore is drained or imbibed when the capillary pressure is above or below the capillary threshold pressure for drainage P_c^D or imbibition P_c^I respectively. Due to the randomness in the local geometry of the porous medium, P_c^D and P_c^I are not fixed values. As discussed by Auradou *et al.* [9] they will vary independently from pore to pore according to their respective distribution function. Furthermore these distributions are isotropic.

Clusters of length $l_y < l^*$ are observed both from experiment and simulation to migrate only small distances in the porous matrix. Usually they get trapped, and can only be re-mobilized by coaleasing with larger migrating clusters. Migration is the process where drainage is followed by imbibition so that a cluster moves without changing its volume. However when these clusters do migrate, their l_y-extension is too small for the viscous pressure field to strongly influence the isotropy of the P_c^D and P_c^I distribution. It is thus equally probable that the cluster will migrate in the l_x-direction as in the l_y-direction. Clusters at these sizes will therefore have an equal extention length in the two directions on the average.

If we now consider a larger cluster of length $l_y > l^*$, the capillary pressure difference along the cluster perimeter will be of importance. Thus pore invasion are most likely to take place in the direction of flow, i.e drainage will occur in pores at the tip of the cluster while pores at the tail will be considered for imbibition. Since the cluster is migrating in the direction of flow, it is also most likely to coalease with smaller trapped clusters at its tip rather than towards the sides, all of which contributes to elongating the cluster in the l_y-direction.

As we have seen, clusters cannot grow infinitely large. It is the occurrence of snap-offs [9] of the cluster tail, caused by imbibition, that will determine the l_y-extension. The probability of a cluster snap-off will mainly depend on; 1) the difference between the average capillary pressure threshold for drainage and imbibition $\bar{P}_c^D - \bar{P}_c^I$ and 2) the capillary pressure difference ΔP_{cap} between pores. Further, snap-offs will typically occur when

$$\Delta P_{\text{cap}} > \bar{P}_c^D - \bar{P}_c^I, \tag{17}$$

from which it follows:

$$\frac{\Delta P_{ss}}{L} l_y > \bar{P}_c^D - \bar{P}_c^I \tag{18}$$

$$l_y > \frac{\left(\bar{P}_c^D - \bar{P}_c^I\right) L}{\Delta P_{ss}} \propto \frac{L}{\Delta P_{ss}} \ . \tag{19}$$

Eq. (19) predicts a cut-off length, dependent on the pressure difference ΔP_{ss}, over which clusters can stay connected. This is, as will become apparent at the end of this section, consistent with our experimental findings.

We have already discussed the normalised probability distribution of non-wetting clusters, $P(s)$, which was shown to obey a scaling law in the cut-off cluster size s^* (Eq. (10)), and thus also in the tuning parameter Q_w (Eq. (9)). We now turn to a discussion of the distribution of l_i for all s, namely the marginal distribution $P(l_i)$. Since there is no *one-to-one* correspondence between l_i and s, no exact (Authors Note: to strong a statement?) analytical solution of $P(l_i)$ can be obtained from Eq. (8). However, $P(l_i|s)$ is Gaussian (Fig. 9a) and narrowly peaked around $\langle l_i \rangle$ (Eq. (13)). On this basis we would expect $P(l_i)$ to have similarities with the distribu-

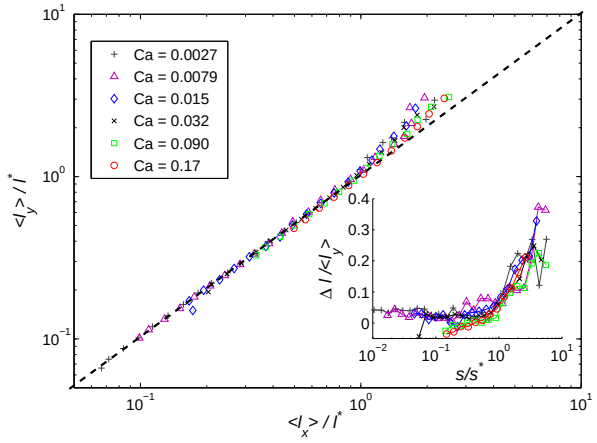

FIG. 10: *Average extension length* $\langle l_x \rangle$ *vs.* $\langle l_y \rangle$*, both axes rescaled with the cut-off length* l^**. Clusters are not elongated, on the average, until* l^* *is reached. Inset shows the relative length difference* $\Delta l/\langle l_y \rangle$ *as a function of* s/s^**, where* $\Delta l = \langle l_y \rangle - \langle l_x \rangle$*.* $\Delta l/\langle l_y \rangle$ *increases significantly when* s^* *is reached.*

tion function

$$f(l) = P(s)\frac{ds}{dl} \tag{20}$$

$$f(l) \propto l^{-\phi} \exp\left[-\left(\frac{l}{l^*}\right)^{\frac{1}{\beta_i}}\right], \tag{21}$$

where

$$\phi = \frac{\tau + \beta_i - 1}{\beta_i} = 2.84\ . \tag{22}$$

The function $f(l)$ is thus the distribution obtained when assuming Eq. (12) applies for all l_i.

The distributions $P(l_y)$ and $P(l_x)$ are plotted in Fig.11a, and it is evident that a cut-off behaviour is dominant, similar to what is found for $P(s)$. Furthermore, for the largest extension lengths, the probability density $P(l_y)$ is larger than $P(l_x)$ for all the Ca-numbers. This is intrinsically linked to the fact that large clusters are elongated in the direction of flow as discussed previously. We have already argued that there exist a cut-off length l^* common for both l_i-directions. The observed difference between $P(l_x)$ and $P(l_y)$ is thus due to different cut-off behaviour in these distributions as a consequence of elongation.

On the basis of Eq. (21) a re-scaling of the form $l^{*\phi}P(l_i)$ vs. l_i/l^* is predicted. The corresponding data collapse is shown in Fig. 11b. The exponent ϕ is in this case taken as the value giving the best collapse, and it is found that $\phi = 2.8 \pm 0.3$, in agreement with Eq. (22). Apart from the crossover at smaller extension lengths the collapse is very good. The small difference in the cutoff function, as discussed above, for the largest extension lengths are indicated by the two solid lines in Fig. 11b. Analog to Eq. (10), $P(l_i)$ obeys the scaling function

$$P(l_i) \propto l^{*-\phi} G_i(l_i/l^*), \tag{23}$$

for clusters above the lower cutoff scale.

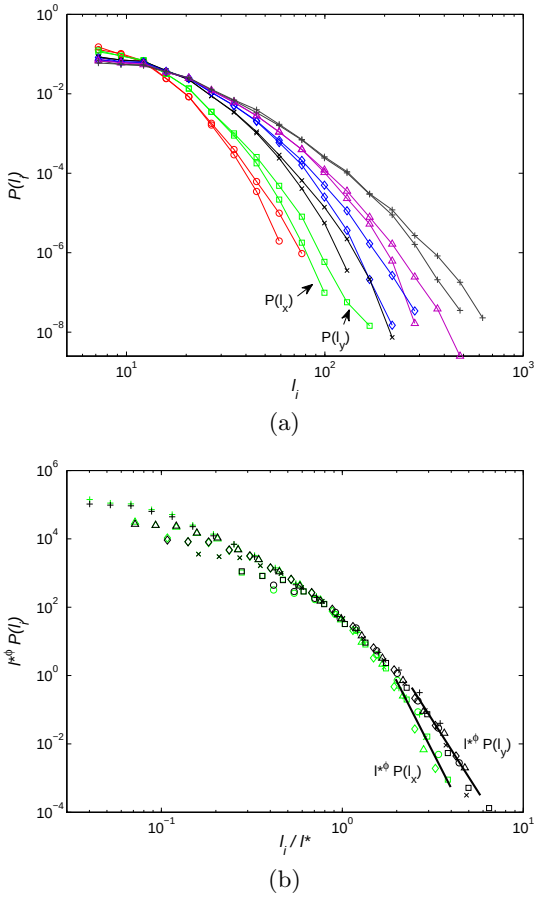

FIG. 11: ***(a)*** *plot of the linear extension distributions* $P(l_x)$ *and* $P(l_y)$ *for various Ca-numbers.* ***(b)*** *shows a data-collapse, predicted by Eq. (21), of the same curves. The exponent* ϕ *is taken as the value that gives the best collapse, and it is found that* $\phi = 2.8 \pm 0.3$*. Solid lines indicate the difference in cutoff function of* $P(l_x)$ *and* $P(l_y)$*.*

At this point an important observation is made; from Eqs. (6,14) the cut-off length l^* is seen to be inversely proportional to the average pressure gradient $\Delta P_{ss}/L$, provided $\beta = \gamma\beta_i$. All of the latter exponents have uncertainty, within we can make the reasonable claim that they are equal, and thus that our findings are consistent with respect to this:

$$l^* \propto \frac{L}{\Delta P_{ss}} \propto Q_w^{-\beta}\ , \tag{24}$$

where β has the value found in Eq. (7). From Eq. (24) it is seen that the cut-off length of non-wetting clusters during steady-state, is set by the viscous pressure field, consistent with Eq. (19).

D. Compressibility effects

There is one important aspect of the cluster dynamics that has not yet been discussed; namely compressibility of the non-wetting phase (air), due to the high pressures involved. As an example, for Ca = 0.17 it is seen from Fig. 3 that the inlet pressure during steady-state is $\sim 55\,\mathrm{kPa}$. This means that air, entering the model at this pressure, has a compressed volume of roughly $\sim 2/3$ relative to that at a pressure of $\sim 5\,\mathrm{kPa}$, found at the outlet. The question is to what extent air compressibility affects the flow dynamics and structure, i.e. compared to the flow of two incompressible fluids.

The produced mass of wetting fluid from the outlet tube is measured during the experiments. From these measurements it is found that in the transient state, i.e. $t < t_{ss}$, the total invasion flow-rate Q_{tot}^{inv} was constant, with values listed in Table I. It is also clear from Table I that $Q_{tot}^{inv} < 15Q_0$, which is direct evidence of air-compressibility. However as steady-state is reached, i.e. $t \geq t_{ss}$, we expect a total flow-rate of $Q_{tot} = 15Q_0$. At this point the pressures are relaxed at a constant average value, and the air is not compressed any further, meaning that a flow-rate of Q_0 is obtained from all seven air-filled syringes.

It is not a trivial question how the compressed air expands as it moves towards lower pressure in the porous medium. Analysis during steady-state has shown that no gradient exists in the direction of flow neither for the non-wetting fluid saturation nor for the distribution of non-wetting clusters. In this respect the air clusters behave as if incompressible, which is an important result.

We claim that most of the expansion of compressed air happens during short time intervals through avalanches in the porous medium. In the following a qualitative description will be given. This phenomenon is a study in its own respect, and a quantitative analysis is beyond the scope of this paper.

From visual inspection it is observed that air is frequently blocked out by the local configuration of wetting fluid around one or more of the air inlet nodes. This causes further compression and thereby a pressure increase in the air tubes. As the pressure continues to increase, the air is seen to slowly displace the blocking wetting fluid. At some point an avalanche of expanding air is triggered (self-reinforcing process?!) and the air and inlet pressure drops abruptly. The avalanche is characterised by channels, not more than a pore size wide, created between existing non-wetting clusters. The temporarily existing non-wetting cluster is narrow in the l_x-direction but spans the air invaded region in the l_y-direction. This means that an avalanche cluster reaches from the originating inlet node to either the displacement front or all the way through the model, dependent on whether the system is in the transient- or steady-state respectively. During an avalanche in the transient state, air is seen to propagate rapidly to the displacement front where it expands surrounded only by the wetting fluid. This rapid propagation of expanding air is also seen in steady-state but the air is now immediately transported to the model outlet. The timescale of an avalanche is of the order of $\sim 1\,\mathrm{s}$, substantially less than in ordinary movement of mobilized non-wetting clusters. During this time, a signature of the avalanche is seen as a spike in the pressure signal from the middle and outlet pressure sensor (Fig. 4). As the pressure inside the avalanche cluster relaxes, the interconnecting channels are imbibed by the surrounding wetting fluid and the displacement now returns to "normal". By normal displacement we mean the fragmented bubble dynamics described in Sec. IV. Being a highly dynamical phenomena, the flow of expanding air in avalanches is visually striking. Fig. 12 shows an avalanche through the central part of the model, also compared to normal displacement during the same time interval.

V. CONCLUSION

Simultaneous two-phase flow in porous media has been studied experimentally, in a large quasi two-dimensional laboratory model of roughly $\sim 10^5$ pores. Both the transient- and steady-state have been considered.

In all experiments the combination of glycerol/water and air have been used as the pair of wetting and non-wetting fluid respectively. Analysis has been performed on the basis of digital imaging of displacement structures and pressure measurements.

The mixed displacement structure of wetting and non-wetting fluid is utterly more complex than what is found in the transient regimes of e.g. capillary or viscous fingering. Due to the simultaneous flow of high viscous wetting fluid, clusters of low viscous non-wetting fluid will be snapped off from the inlet nodes. The competition of both drainage and imbibition causes fragmentation of the non-wetting fluid, and the dynamics are characterized by the movement and mixing of discreet non-wetting clusters in a background field of wetting fluid. Initially the fragmentation and mixing of fluids increases, but are seen to stabilize when the most advanced parts of the front has reached roughly halfway through the model. At this point the invasion structure consists of a heterogeneous region at the front and a homogeneous region further behind, locally in steady-state, similar to that of later global steady-state. This is supported by analysis of pressure differences, fluid saturation and statistical properties. It is an important result, because this kind of similarity between a transient and steady regime is far from obvious.

The invasion structure reached breakthrough at a characteristic time t_b, and the system reached steady state at a later time t_{ss}. We have shown that t_b and t_{ss} are proportional to the total invasion flow-rate Q_{tot}^{inv}, and that the time difference between breakthrough and steady-state was 38% of the breakthrough time.

The probability distribution of the size of non-wetting

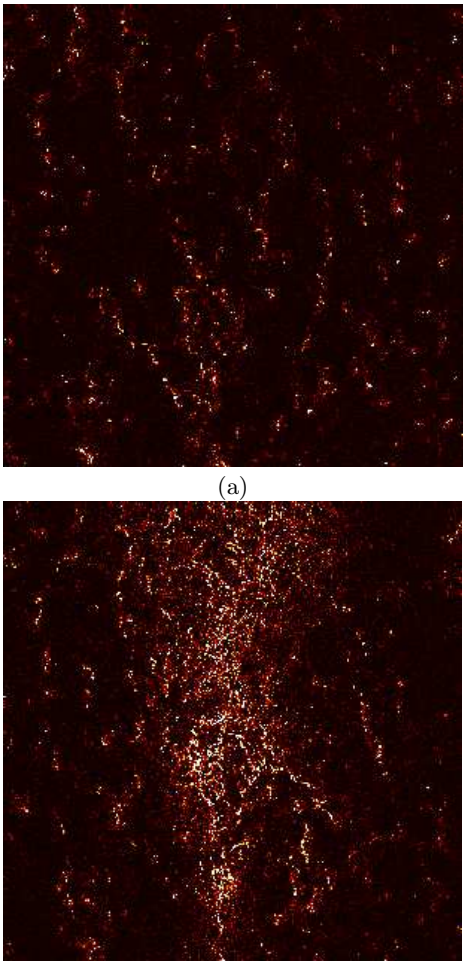

(a)

(b)

FIG. 12: *A central region of the model, (*17×17*)cm consisting of* $\sim 10^4$ *pores, is captured with a fast camera during steady-state (*$Ca = 0.090$*). Flow direction is from top to bottom. By subtracting two images of the displacement structure, separated in time by* $\Delta t \sim 1\,s$*, pores imbibed or drained (bright regions) during this time can be distinguished from pores of unchanged fluid configuration (dark regions). (**a**) Normal displacement. Pore fluid configurations are close to unchanged during* Δt*. (**b**) avalanche through the same region as depicted in (a). In this case the fluid configurations are drastically changed in a narrow central part of the image during* Δt *as the avalanche passes through. This is the signature of air expanding rapidly through the region.*

clusters exhibits a clear cutoff for all Ca-numbers investigated during steady-state. No powerlaw behavior is found, however for larger clusters reasonable fits are obtained to Eq. (8). We find $\tau \approx 2$ and that the cutoff cluster size s^* is roughly inversely proportional to the wetting fluid flow-rate Q_w. The obtained value for τ is close to the value found in percolation theory, but we emphasize again that it is not determined with a high degree of certainty in our case. Finally, the rescaling predicted by Eq. (8) is seen from Fig. 8b to produce a very good data collapse of the size distributions.

In a recent paper by Ramstad & Hansen [7], cluster size distributions during steady-state two-phase flow in a porous medium was studied numerically for $M = 1$, i.e. viscosity match of the fluid pair. They found that below a critical value of the non-wetting fluid saturation, the non-wetting cluster size distribution were dominated by a cutoff behaviour similar to what have been presented here. Above the critical saturation value, power-law behaviour was observed. Due to the large difference in viscosity contrast between our experiments and these simulations, no direct comparison can be made. Nevertheless it would be interesting to perform future experiments with the intention of exploring such a critical value.

Through the method of bounding boxes we have been able to study cluster extension in the l_x- and l_y-direction, i.e. transverse and parallel to the direction of flow respectively. We find that for a given cluster size, the distribution of extension lengths is a Gaussian with a standard deviation of 22% of the mean value. Additionally a scaling is found between the mean extension length $\langle l_i \rangle$ and s, equal in both directions with the exponent $\beta_i \approx 0.57$, valid up to s^*. Clusters at these sizes are thus isotropic. Clusters above s^* are elongated in the direction of flow, due to the an-isotropic influence of the viscous pressure field as argued.

From the scaling of $\langle l_i \rangle$ with s and the scaling of s^* with Q_w, we obtain the important result that the cutoff length l^* is a power-law in Q_w with the exponent $\gamma\beta_i \approx \beta_i$. This is consistent with the flow-rate dependence of the measured pressure difference during steady-state ΔP_{ss}. This pressure difference follows a power-law in the wetting fluid flow-rate Q_w with an exponent $\beta \approx 0.57$. It is thus experimentally verified that the cutoff size of non-wetting clusters is determined by the viscous pressure field of wetting fluid.

From our findings in this study, we would like in the future to consider any history dependence of global steady-state, since true steady-state does not depend on initial transients. Additionally, experiments should be performed where tuning the wetting fluid flow-rate independently from the non-wetting fluid flow-rate. At present time, preliminary results indicate that the flow dynamics show no strong dependence of the latter flow parameter. Finally, a theoretical prediction of our presented results and observations cannot be found in the existing literature and are thus warranted.

Acknowledgments

The work supported by...

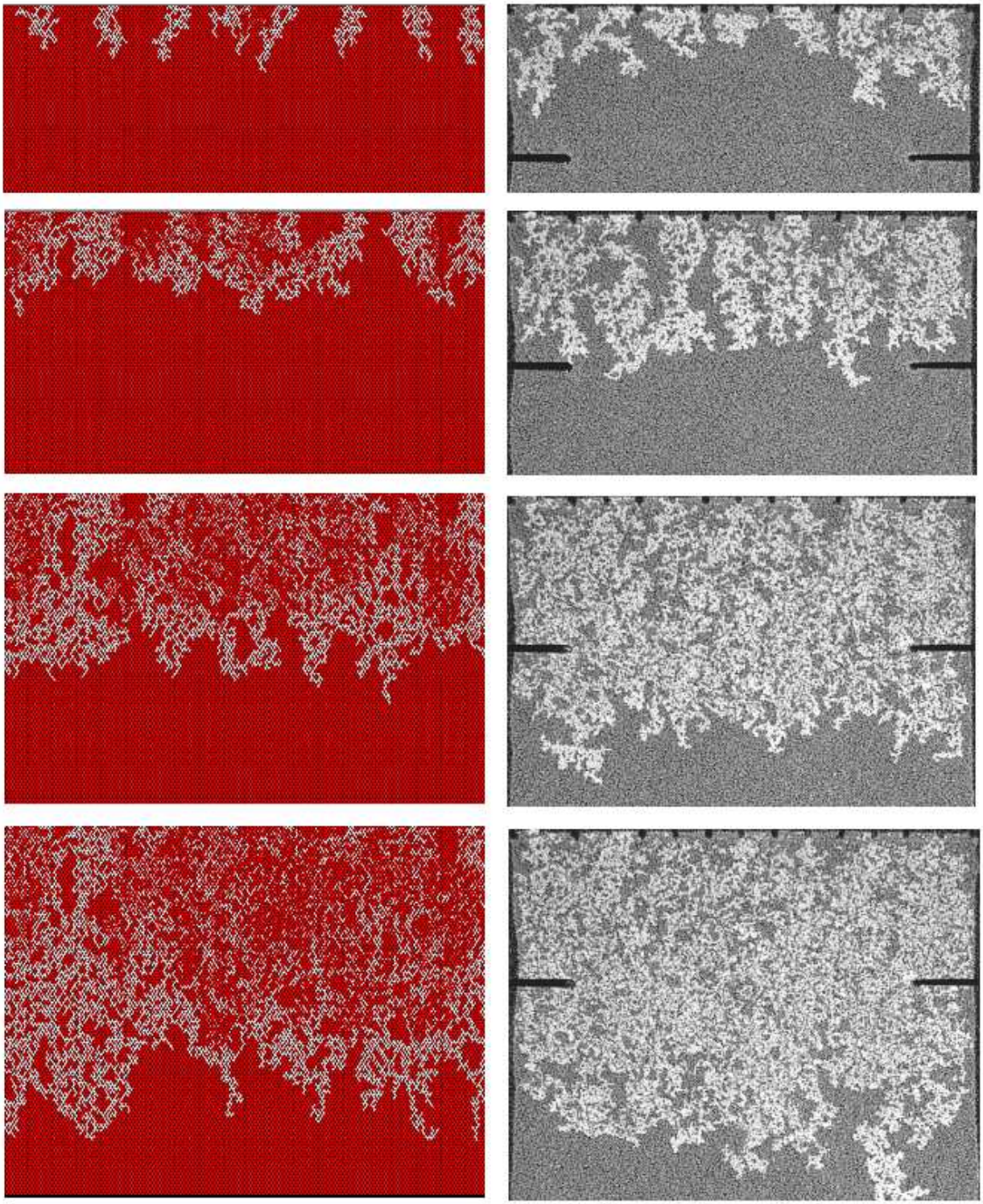

FIG. 13: Time evolution of the transient displacement process. Left – simulation, right – experiment. Both fluids are injected at the top of the images (i.e. the flow direction is from top to bottom.)

[1] O. I. Frette, K. J. Måløy, J. Schmittbuhl, and A. Hansen, Phys. Rev. E **55**, 2969 (1997).
[2] G. Løvoll, Y. Meheust, R. Toussaint, J. Schmittbuhl, and K. J. Måløy, Phys. Rev. E **70** (2004).
[3] Y. Meheust, G. Løvoll, K. J. Måløy, and J. Schmittbuhl, Phys. Rev. E (2002).
[4] E. Aker, K. J. Måløy, A. Hansen, and G. G. Batrouni, Transport in Porous Media **32**, 163 (1998).
[5] H. A. Knudsen, E. Aker, and A. Hansen, Transport in Porous Media **47**, 99 (2002).
[6] H. A. Knudsen and A. Hansen, Phys. Rev. E **65**, 056310 (2002).
[7] T. Ramstad and A. Hansen, Phys. Rev. E **73**, 026306 (2006).
[8] D. Stauffer and A. Aharony, *Introduction to Percolation Theory* (Taylor & Francis, London, 1992).
[9] H. Auradou, K. J. Måløy, J. Schmittbuhl, and A. Hansen, Transport in Porous Media **50**, 267 (2003).